Electronic and magnetic properties of iridium ilmenites math xmlns="http://www.w3.org/1998/Math/MathML">mrow>mi>A/mi>msub>mi>IrO/mi>mn>3/mn>/msub>/mrow>/math> math xmlns="http://www.w3.org/1998/Math/MathML">mrow>mo>(/mo>mi>A/mi>mo>=/mo>mi>Mg/mi>mo>,/mo>mo> /mo>mi>Zn/mi>mo>,/mo>mo> /mo>mi>and/mi>mo> /mo>mi>Mn/mi>mo>)/mo>/mrow>/math>

Seong-Hoon Jang and Yukitoshi Motome

Phys. Rev. Materials **5**, 104409 — Published 20 October 2021
DOI: 10.1103/PhysRevMaterials.5.104409

Electronic and magnetic properties of iridium ilmenites AIrO$_3$ (A = Mg, Zn, and Mn)

Seong-Hoon Jang and Yukitoshi Motome
Department of Applied Physics, University of Tokyo, Tokyo 113-8656, Japan

(Dated: August 25, 2021)

We theoretically investigate the electronic band structures and magnetic properties of ilmenites with edge-sharing IrO$_6$ honeycomb layers, AIrO$_3$ with A = Mg, Zn, and Mn, in comparison with a collinear antiferromagnet MnTiO$_3$. The compounds with A = Mg and Zn were recently reported in Y. Haraguchi *et al.*, Phys. Rev. Materials **2**, 054411 (2018), while MnIrO$_3$ has not been synthesized yet but the honeycomb stacking structure was elaborated in a superlattice with MnTiO$_3$ in K. Miura *et al.*, Commun. Mater. **1**, 55 (2020). We find that, in contrast to MnTiO$_3$, where an energy gap opens in the Ti 3d bands by antiferromagnetic ordering of the high-spin $S = 5/2$ moments, MgIrO$_3$ and ZnIrO$_3$ have a gap in the Ir 5d bands under the influence of both spin-orbit coupling and electron correlation. Their electronic structures are similar to those in the spin-orbit coupled Mott insulators with the $j_{\rm eff} = 1/2$ pseudospin degree of freedom, as found in monoclinic A_2IrO$_3$ with A = Na and Li which have been studied as candidates for the Kitaev spin liquid. Indeed, we find that the effective exchange interactions between the $j_{\rm eff} = 1/2$ pseudospins are dominated by the Kitaev-type bond-dependent interaction and the symmetric off-diagonal interactions. On the other hand, for MnIrO$_3$, we show that the local lattice structure is largely deformed, and both Mn 3d and Ir 5d bands appear near the Fermi level in a complicated manner, which makes the electronic and magnetic properties qualitatively different from MgIrO$_3$ and ZnIrO$_3$. Our results indicate that the IrO$_6$ honeycomb network in the ilmenites AIrO$_3$ with A = Mg and Zn would offer a good platform for exotic magnetism by the spin-orbital entangled moments like the Kitaev spin liquid.

I. INTRODUCTION

Ilmenite, whose chemical formula is given by ABO$_3$, crystalizes in a trigonal structure with the space group $R\bar{3}$ similar to corundum A_2O$_3$. Both ilmenite and corundum share the layered structure with a honeycomb network of edge-sharing octahedra, but a difference lies in the stacking manner; corundum is composed of a stacking of isostructural AO$_6$ honeycomb layers, but ilmenite is made of an alternative stacking of AO$_6$ and BO$_6$ honeycomb layers, as shown in Fig. 1. While ilmenite is originally the name for a titanium-iron oxide mineral FeTiO$_3$, its relatives, such as NiTiO$_3$, CoTiO$_3$, and MnTiO$_3$, have been studied for a long time as a good playground for two-dimensional magnetism [1–11]. Mixed compounds like (Ni,Mn)TiO$_3$ were also investigated as they exhibit interesting spin glass behavior [11–15]. Later, the titanium antiferromagnets have also attracted the interest from their multiferroics behavior [16, 17] and magnetochiral dichroism [18].

Recently, a new series of ilmenite with B=Ir has been synthesized as MgIrO$_3$, ZnIrO$_3$, and CdIrO$_3$ [19, 20]. These compounds are of particular interest from a different perspective than ATiO$_3$: they have a honeycomb network of edge-sharing IrO$_6$ octahedra similar to monoclinic A_2IrO$_3$ with A = Na and Li which have been intensively studied as candidates for realizing a quantum spin liquid in the honeycomb Kitaev model [21–31]. In A_2IrO$_3$, the 5d levels in Ir^{4+} ions are split by the strong spin-orbit coupling (SOC) into quartet and doublet, and the half-filled doublet is further split by the Coulomb interaction to realize the so-called spin-orbit Mott insulator [32]. Then, the low-energy physics is described by the pseudospin degree of freedom for the Kramers doublet with the effective magnetic moment of $j_{\rm eff} = 1/2$ [33, 34]. Owing to the edge-sharing geometry, the dominant interaction between neighboring $j_{\rm eff} = 1/2$ moments can be highly anisotropic, which gives a realization of the bond-dependent Ising interaction in the Kitaev model [24–27, 35, 36]. Since the iridium ilmenites have a similar honeycomb network, they potentially serve as another candidates for the Kitaev spin liquid. Powder samples of these compounds, however, were shown to exhibit magnetic phase transitions at 31.8 K for MgIrO$_3$, 46.6 K for ZnIrO$_3$ [19], and 90.9 K in CdIrO$_3$ [20], which are higher than $\sim$ 15 K for AIrO$_3$ [22, 23, 37–39]. The susceptibility measurements for the A = Mg and Zn indicate that they have in-plane magnetic anisotropy, while Na$_2$IrO$_3$ and Li$_2$IrO$_3$ show the out-of-plane and in-plane anisotropy, respectively [22, 28]. The estimates of the magnetic moments are consistent with the $j_{\rm eff} = 1/2$ picture, except for CdIrO$_3$ [20]. Despite these interesting aspects, the electronic and magnetic properties of the iridium ilmenites have not been theoretically studied thus far.

In this paper, we investigate the electronic band structures of MgIrO$_3$ and ZnIrO$_3$ by using the first-principles calculations with the fully-relativistic local density approximation including effective onsite Coulomb interactions, called the LDA+SOC+U method. For comparison, we study the well-known antiferromagnetic insulator MnTiO$_3$ and a fictitious crystal MnIrO$_3$ whose local stacking structure was recently elaborated in a superlattice with MnTiO$_3$ [40]. We find that MgIrO$_3$ and ZnIrO$_3$ have similar band structures near the Fermi level to the Kitaev candidates Na$_2$IrO$_3$ and Li$_2$IrO$_3$; the SOC and Coulomb interactions act cooperatively to realize the spin-orbit coupled Mott insulating state whose low-energy physics is well described by the pseu-

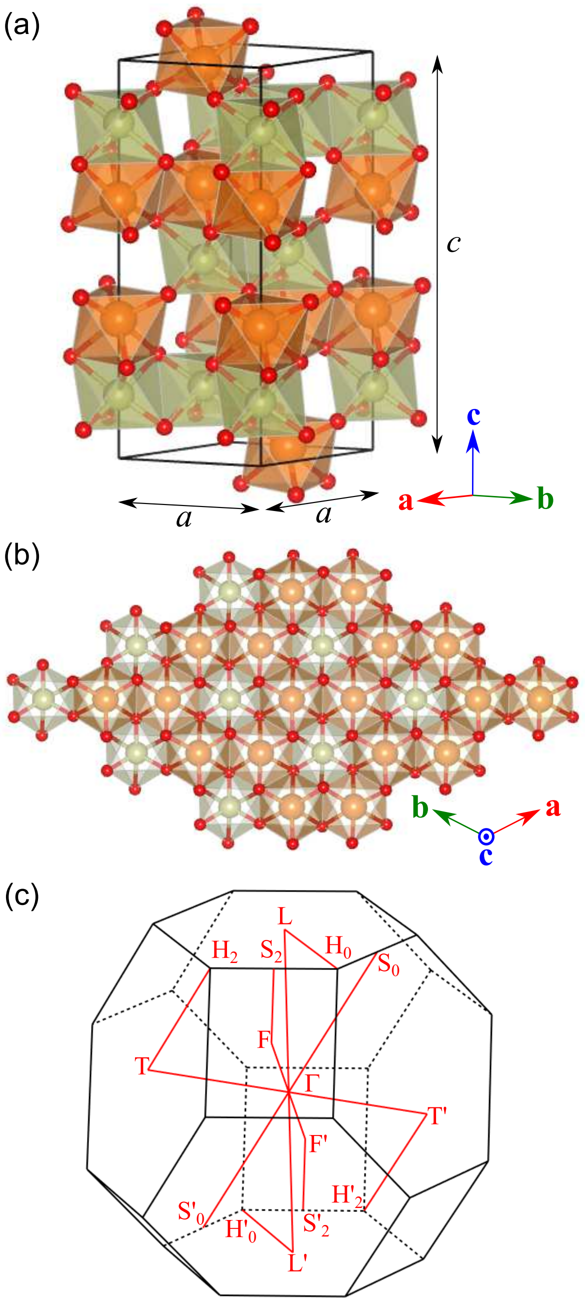

FIG. 1. (a) and (b) Lattice structure of ilmenite ABO_3. The orange and yellow octahedra denote AO_6 and BO_6, each of which form a two-dimensional honeycomb network with edge sharing. The adjacent AO_6 and BO_6 honeycomb layers are stacked with face and corner sharing. (a) Bird's-eye view and (b) projection from the c axis. The black lines in (a) denote the conventional unit cell with the lattice constants, a and c. (c) The first Brillouin zone. The red lines denote the symmetric lines used in the plots of the band structures in Sec. III and Appendix B.

dospin with effective magnetic moment $j_{\rm eff} = 1/2$. This is in contrast to the antiferromagnetic insulating state in $MnTiO_3$, where $(3d)^5$ electrons form the high-spin $S = 5/2$ state by the Hund's-rule coupling and the energy gap is opened by the exchange splitting in the antiferromagnetic state. In $MgIrO_3$ and $ZnIrO_3$, we show that the antiferromagnetic solution has a lower energy than the paramagnetic and ferromagnetic ones, but the antiferromagnetic moment is very small ~ 0.1 $\mu_{\rm B}$~~, implying that the $j_{\rm eff} = 1/2$ moments suffer from frustration~~. Furthermore, by constructing a multiorbital Hubbard model from the maximally-localized Wannier functions (MLWFs) [41, 42] and performing the perturbation expansion from the atomic limit, we show that the exchange interactions between the $j_{\rm eff} = 1/2$ pseudospins are described by the dominant Kitaev-type bond-dependent one and the subdominant symmetric off-diagonal ones. The results indicate that the edge-sharing honeycomb network of IrO_3 octahedra in $MgIrO_3$ and $ZnIrO_3$ would offer a good playground for spin-orbital entangled magnetism toward the Kitaev spin liquid. On the other hand, we find that the optimized lattice structure of $MnIrO_3$ is largely deformed from those for $MnTiO_3$, and the band structure near the Fermi level is complicated including both Mn $3d$ and Ir $5d$ contributions.

The structure of this paper is as follows. In Sec. II, we describe the details of the LDA+SOC+U calculations and the method to estimate the effective exchange coupling constants. In Sec. III, we present our results for $MnTiO_3$ (Sec. III A), $MgIrO_3$ and $ZnIrO_3$ (Sec. III B), and $MnIrO_3$ (Sec. III C). In Sec. III B, we discuss the electronic band structure in Sec. III B 1, the transfer integrals in Sec. III B 2, and the effective magnetic interactions in Sec. III B 3. For comparison, we also study the electronic band structure for $MgIrO_3$ by using the Heyd-Scuseria-Ernzerhof (HSE) hybrid functional approach in Appendix A [43]. The results for $ZnIrO_3$ are qualitatively similar to those for $MgIrO_3$, and detailed in Appendix B. Section IV is devoted to the summary.

II. METHOD

The *ab initio* calculations are performed by using `Quantum ESPRESSO` [44]. We adopt the fully-relativistic and non-relativistic projector-augmented-wave-method Perdew-Zunger type pseudopotentials for the A and B-site ions and the O ligands, respectively [45–47]. While we employ the experimental structural data for $MnTiO_3$ [48] and for $MgIrO_3$ and $ZnIrO_3$ [19], we perform structural optimization for the fictitious compound $MnIrO_3$ starting from the experimental structure for $MnTiO_3$ with replacement of Ti by Ir; we relax not only the atomic positions within the primitive unit cell but also the lattice translation vectors. In the optimization, we set the minimum ionic displacement to 0.001 Å in the Broyden-Fletcher-Goldfarb-Shanno iteration scheme [49]. Afterwards, we symmetrize the optimal structure within the trigonal space group $R\bar{3}$, where the residual stress is less than 30 kbar. In all the calculations, we take the primitive unit cell, and $4 \times 4 \times 4$ and $8 \times 8 \times 8$

Monkhorst-Pack **k**-grids for self-consistent field and non self-consistent field calculations, respectively [50]. We set the convergence threshold for the self-consistent field calculations to 10^{-10} Ry. The kinetic energy cutoff is set to 200 Ry for all the cases. In the LDA+SOC+U calculations, we include the Hubbard correction to the Mn $3d$ and Ir $5d$ orbitals with the Coulomb repulsion $U = U_{\mathrm{Mn}}$ and U_{Ir}, respectively, together with the Hund's-rule coupling J_{H}, by assuming $J_{\mathrm{H}}/U = 0.1$ in the rotationally invariant scheme [51]. For comparison, we also perform the calculations for $\mathrm{MgIrO_3}$ by using HSE hybrid functional; see Appendix A for the details.

We construct the MLWFs of Ir $5d$ t_{2g} and O $2p$ orbitals for $\mathrm{MgIrO_3}$ and of Zn $3d$, Ir $5d$ t_{2g}, and O $2p$ orbitals for $\mathrm{ZnIrO_3}$ for the obtained electronic band structures by using `WANNIER90` [42]. Note that, in most of the previous studies for other Kitaev candidate materials, the MLWF analyses were performed only for the $5d$ or $4d$ t_{2g} orbitals [24, 26, 27, 52, 53]. In the present study, however, we include O $2p$ for both $\mathrm{MgIrO_3}$ and $\mathrm{ZnIrO_3}$ and also Zn $3d$, since we find that they overlap with Ir $5d$ t_{2g} (see Sec. III B and Appendix B). From the results, we calculate the projected density of states (DOS) for each MLWF orbital. For the Ir $5d$ t_{2g} orbitals, we also compute the DOS projected onto the spin-orbital coupled bases labelled by the effective angular momentum j_{eff}.

Then, we estimate the effective transfer integrals between the Ir t_{2g} orbitals by using the MLWFs for the $U_{\mathrm{Ir}} = 0$ case; the effective transfer integral between d orbital u with spin σ at site i and d orbital v with spin σ' at the neighboring site i' is calculated as

$$\tilde{t}_{iu\sigma,i'v\sigma'} = t_{iu\sigma,i'v\sigma'} + \sum_{o,p,\sigma_p} \frac{t_{iu\sigma,op\sigma_p} t^{*}_{i'v\sigma',op\sigma_p}}{\Delta_{uv\text{-}p} + U_p}, \qquad (1)$$

where the first term $t_{iu\sigma,i'v\sigma'}$ denotes the d-d direct hopping, and the second term describes the d-p-d indirect hoppings via oxygen $2p$ orbitals with spin σ_p at ligand site o between i and i' in the second-order perturbation manner. $\Delta_{uv\text{-}p}$ denotes the harmonic mean of the energies of orbitals u and v measured from that of p, and U_p represents the Coulomb interaction in the $2p$ orbitals. Here, U_p is taken into account, considering less screening in the present MLWF analyses including the O $2p$ orbitals (see Sec. III B 3). For the further-neighbor transfers, we add d-p-p-d indirect hoppings in the third-order perturbation manner.

Finally, we construct the multiorbital Hubbard models for the Ir t_{2g} orbitals, which are composed of the kinetic hopping term, the crystal-field splitting, the SOC coupling, and the Coulomb interactions, as discussed in detail in Ref. [27], and perform the perturbation expansion from the strong limit of the Coulomb interactions in terms of the effective transfer integrals to derive the effective Hamiltonian for the $j_{\mathrm{eff}} = 1/2$ pseudospins of the Ir ions. Only the difference from Ref. [27] lies in the computation of the effective transfer integrals where we take into account the oxygen $2p$ orbitals explicitly. Note that a similar scheme was used for the f-electron cases of Refs. 54 and 55.

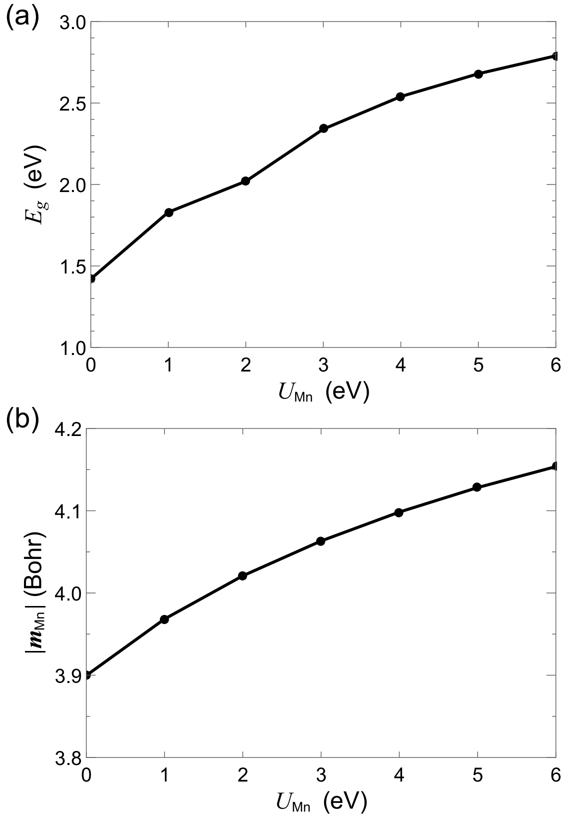

FIG. 2. (a) The energy gap and (b) the antiferromagnetic moment at the Mn site in the c-AFM state in $\mathrm{MnTiO_3}$ as functions of the Coulomb repulsion at the Mn site, U_{Mn}, obtained by the LDA+SOC+U calculations.

III. RESULT

A. $\mathrm{MnTiO_3}$

Before going into the iridium ilmenites, we start with the well-known $\mathrm{MnTiO_3}$ as a reference. This compound is an antiferromagnetic insulator with a collinear Néel order along the c axis, which we call the c-AFM state hereafter [4]. The energy gap is estimated as $\simeq 3.18$ eV [56], and the magnetic moment is estimated as $\simeq 4.55$ μ_{B} [4], which is consistent with the high-spin state of Mn^{2+} ions with $S = 5/2$ under the strong Hund's-rule coupling. The electronic band structure was studied by the *ab initio* calculations with the generalized gradient approximation, and the AFM nature was reproduced [57].

We here perform the LDA+SOC+U method while changing the Coulomb repulsion at the Mn site, U_{Mn}. We find that the antiferromagnetic state has a lower energy compared to the paramagnetic and ferromagnetic solutions, while the energy does not depend so much on

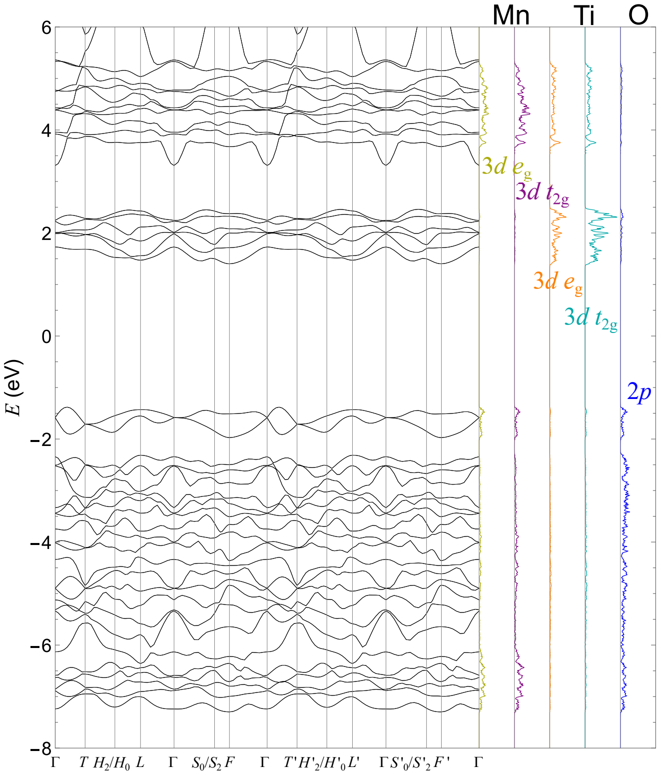

FIG. 3. Electronic band structure of $\mathrm{MnTiO_3}$ obtained by the LDA+SOC+U calculations for the c-AFM state at $U_{\mathrm{Mn}} = 6$ eV. The right panels display the projected DOS for the relevant orbitals in each ion. The Fermi level is set to zero.

the direction of the antiferromagnetic moments; the energy difference between the states with in-plane and out-of-plane moments is smaller than 0.1 meV per unit cell for all U_{Mn} (Here and hereafter, all the energies are measured per unit cell.). Hence, in the following calculations, we assume the c-AFM state which is observed experimentally [4]. The c-AFM state is insulating even in the absence of U_{Mn}; the energy gap E_g and the magnitude of the antiferromagnetic moment $|\mathbf{m}_{\mathrm{Mn}}|$ are estimated as $\simeq 1.4$ eV and $\simeq 3.9\ \mu_{\mathrm{B}}$, respectively, at $U_{\mathrm{Mn}} = 0$. Both E_g and $|\mathbf{m}_{\mathrm{Mn}}|$ increase with U_{Mn}, as plotted in Fig. 2. We note that both values of E_g and $|\mathbf{m}_{\mathrm{Mn}}|$ are slightly smaller than the experimental estimates but approach them for large U_{Mn}. The large value of $|\mathbf{m}_{\mathrm{Mn}}|$ indicates that the antiferromagnetic moment is composed of the high-spin $S = 5/2$ state of the Mn ions under the strong Hund's-rule coupling, consistent with the experiment.

Figure 3 shows the electronic band structure of $\mathrm{MnTiO_3}$ in the c-AFM state with $U_{\mathrm{Mn}} = 6$ eV. The energy gap opens between the occupied states dominated by the Mn 3d and O 2p hybridized bands and the unoccupied states dominated by the Ti 3d bands. See the projected DOS in the right panels of Fig. 3. The Mn 3d bands are largely split by the exchange energy from the c-AFM order.

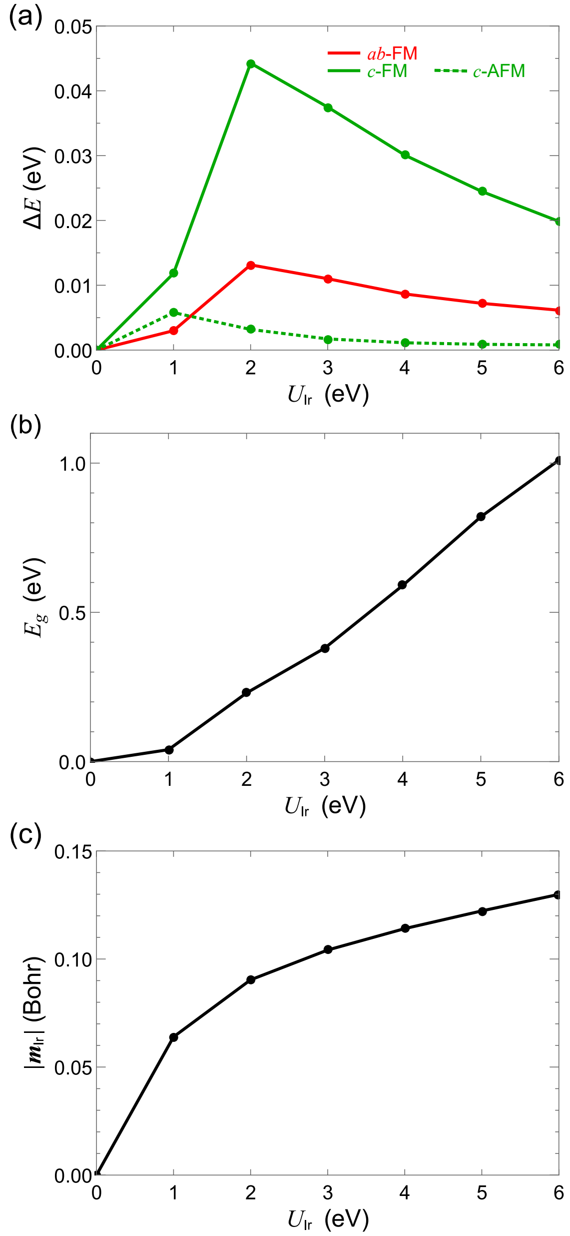

FIG. 4. (a) Energy measured from the ab-AFM state in $\mathrm{MgIrO_3}$ as a function of the Coulomb repulsion at the Ir site, U_{Ir}, obtained by the LDA+SOC+U calculations. (b) The energy gap and (c) the antiferromagnetic moment at the Ir site in the ab-AFM state.

B. MgIrO$_3$ and ZnIrO$_3$

1. Electronic structure

Let us turn to the iridium ilmenites $\mathrm{MgIrO_3}$ and $\mathrm{ZnIrO_3}$. Since the two compounds have similar electronic band structures, we focus on $\mathrm{MgIrO_3}$ in this section and present the results for $\mathrm{ZnIrO_3}$ in Appendix B.

In $\mathrm{MgIrO_3}$, the lowest-energy state among the different magnetic states which we calculated is the antiferromagnetic state whose moments lie in the ab plane. In principle, the energy depends on the direction of the magnetic moments within the plane, but we do not find any significant energy change by rotating the direction (the energy difference between the states whose moments are parallel and perpendicular to one of the Ir-Ir bond directions is less than 0.2 meV for all values of the Coulomb interaction at the Ir site, U_{Ir}, calculated here). Hence, we measure the energy from the state with moments parallel to the bonds, which we call the ab-AFM state, and plot the result in Fig. 4(a). We find that the ab-AFM state has the lowest energy in the whole range of U_{Ir}, except for $U_{\mathrm{Ir}} = 0$ where the system is a paramagnetic metal (see below). The result is consistent with the experiment where the magnetic susceptibility shows the easy-plane anisotropy [19]. We note, however, that the energy difference between the ab-AFM and c-AFM state is not large and becomes smaller for larger U_{Ir}.

In Figs. 4(b) and 4(c), we show the results of the energy gap E_g and the magnitude of the magnetic moment of the Ir ion, $|\mathbf{m}_{\mathrm{Ir}}|$, as functions of U_{Ir}. When $U_{\mathrm{Ir}} = 0$, we obtain $E_g = 0$ and $|\mathbf{m}_{\mathrm{Ir}}| = 0$, indicating that the system is a paramagnetic metal. The band structure is shown in Fig. 5. The relevant bands near the Fermi level are dominated by the Ir $5d$ states, which are composed of the lower-energy $j_{\mathrm{eff}} = 3/2$ and higher-energy $j_{\mathrm{eff}} = 1/2$ states split by the SOC, as shown in the projected DOS in the right panels of Fig. 5. The Fermi level lies in the $j_{\mathrm{eff}} = 1/2$ bands; the two bands in the $j_{\mathrm{eff}} = 1/2$ manifold overlap slightly near the Fermi level, forming the metallic state, as shown in the enlarged plot in Fig. 5(b).

When we switch on U_{Ir}, the system turns into the ab-AFM insulating state, as shown in Figs. 4(b) and 4(c). While E_g increases almost linearly with U_{Ir}, the gap value is relatively small compared to that for the $3d$ compound $\mathrm{MnTiO_3}$ in Fig. 2(a). In addition, $|\mathbf{m}_{\mathrm{Ir}}|$ grows slowly with U_{Ir} and has a small value of $|\mathbf{m}_{\mathrm{Ir}}| \simeq 0.1\ \mu_{\mathrm{B}}$. The band structure of the ab-AFM insulating state is shown in Fig. 6 at $U_{\mathrm{Ir}} = 3$ eV. In the ab-AFM state, the energy gap is opened by U_{Ir} between the two $j_{\mathrm{eff}} = 1/2$ bands, while the $j_{\mathrm{eff}} = 3/2$ bands slightly hybridize with them. This is a typical electronic band structure of the spin-orbit coupled Mott insulator, common to the Kitaev candidate materials like $A_2\mathrm{IrO_3}$ (A = Na and Li) and α-$\mathrm{RuCl_3}$ [24, 29, 33, 34, 58–61]. The results suggest that the small magnetic moment in the ab-AFM state arises from the spin-orbit entangled moments described by the $j_{\mathrm{eff}} = 1/2$ pseudospin degree of freedom.

For comparison, we also study the electronic band structure by using the HSE hybrid functional, which includes the electron correlations in a different manner from the LDA+SOC+U method; see Appendix A. The band structure and the projected DOS are similar to the results for U_{Ir} = 2-3 eV obtained the LDA+SOC+U calculation. This supports our conclusion on the electronic state discussed above.

$\mathrm{ZnIrO_3}$ shows similar behaviors; see Appendix B. A difference from $\mathrm{MgIrO_3}$ observed in our calculations is that the ab-AFM state has a slightly higher energy than the c-AFM state, which is not compatible with the experiment [19]. Nonetheless, the electronic band structure indicates that this compound is also categorized into a spin-orbit coupled Mott insulator with the active $j_{\mathrm{eff}} = 1/2$ pseudospins, similar to $\mathrm{MgIrO_3}$.

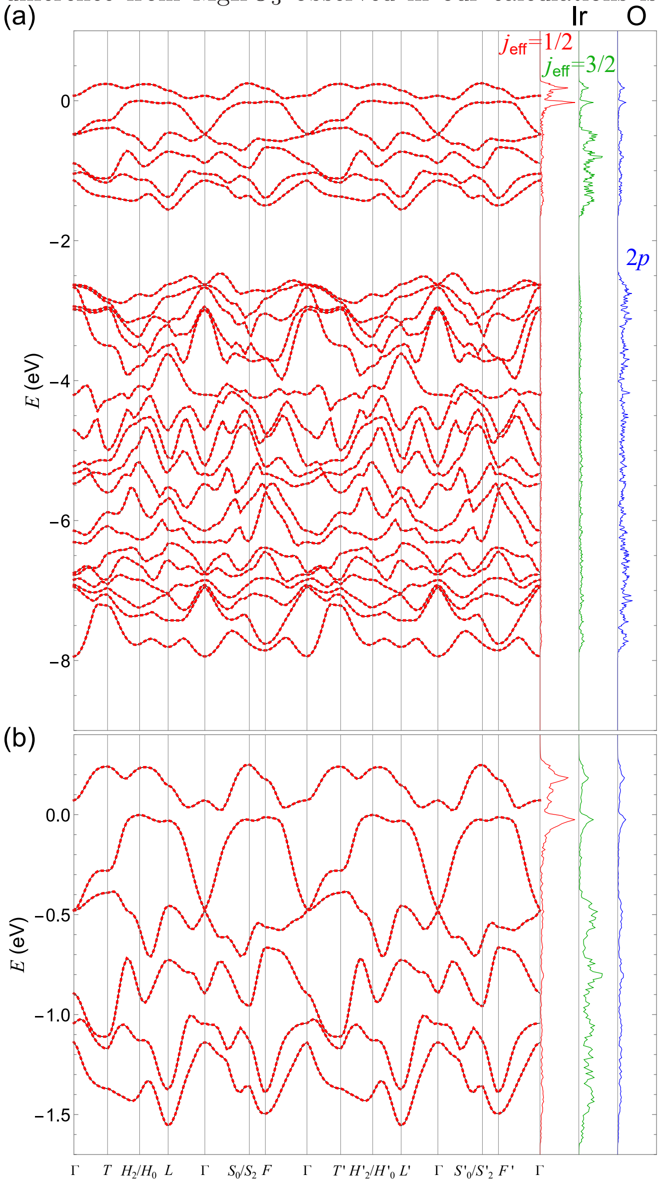

FIG. 5. The electronic band structure of $\mathrm{MgIrO_3}$ obtained by the LDA calculations ($U_{\mathrm{Ir}} = 0$) for the paramagnetic metallic state. The black curves denote the LDA results and the red dashed ones represent the band dispersions obtained by tight-binding parameters estimated by the MLWFs. The right panels display the projected DOS for each orbital. The Fermi level is set to zero.

2. *Transfer integrals*

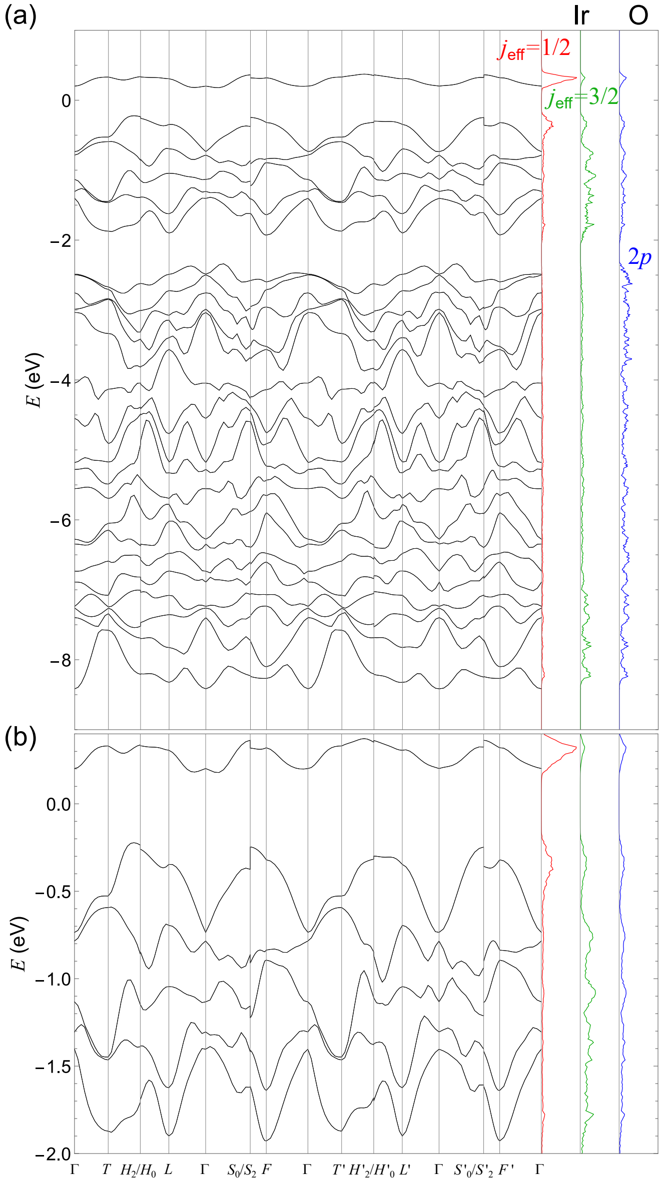

FIG. 6. The electronic band structure of $\mathrm{MgIrO_3}$ obtained by the LDA+SOC+U calculations for the ab-AFM state with $U_{\rm Ir} = 3$ eV. The notations are common to those in Fig. 5.

To examine whether the iridium ilmenites have dominant Kitaev-type bond-dependent interactions between the $j_{\rm eff} = 1/2$ pseudospins, we first perform the MLWF analysis for the case of $\mathrm{MgIrO_3}$ by using the band structure at $U_{\rm Ir} = 0$ in Fig. 5. We find that the tight-binding model obtained from the MLWF analysis well reproduce the *ab initio* results, as shown in Fig. 5. Then, following the procedures in Sec. II, we estimate the effective transfer integrals between the Ir t_{2g} orbitals, including both direct and indirect contributions. We present the results for the nearest-neighbor z bond, where the effective Kitaev interaction takes the form of $S_i^z S_j^z$ [see Eq. (2) below], in Table I. Here, we show the estimates obtained by assuming $U_p = 0.0$, 0.5, and 1.0 eV. The values on the x and y bonds are obtained by cyclic permutations of $\{xyz\}$.

As shown in Table I, we find that the most dominant transfer integral is the one between the yz and zx orbitals, which plays an important role in generating the Kitaev-type interaction [62]. We note that the value at $U_p = 0$ is considerably larger compared to those in $A_2\mathrm{IrO_3}$ (A = Na and Li) and α-$\mathrm{RuCl_3}$ [26, 27, 52], but it is rapidly reduced by U_p and becomes comparable to those for $U_p = 1.0$ eV. This appears to justify the inclusion of U_p to compensate the less screening in the present MLWF analysis including the O $2p$ orbitals. The d-p en-

TABLE I. Transfer integrals between the Ir t_{2g} orbitals on the nearest-neighbor z bond for $\mathrm{MgIrO_3}$. The values represent the effective transfer integrals from the orbital and spin in the column to those in the row, which are estimated from the MLWF analysis for the band structure at $U_{\mathrm{Ir}} = 0$ in Fig. 5. In each matrix element, we display three values by assuming $U_p = 0.0$, 0.5, and 1.0 eV from top to bottom; see the text for details. The unit is in meV. The upper-right half of the table is omitted as the matrix is Hermite conjugate.

	$yz\uparrow$	$yz\downarrow$	$zx\uparrow$	$zx\uparrow$	$xy\uparrow$	$xy\uparrow$
$yz\uparrow$	101 126 138					
$yz\downarrow$	0.00 0.00 0.00	101 126 138				
$zx\uparrow$	1450-13.3i 904-12.0i 646-11.1i	2.73i 2.13i 1.72i	101 126 138			
$zx\downarrow$	2.73i 2.13i 1.72i	1450+13.3i 904+12.0i 646+11.1i	0.00 0.00 0.00	101 126 138		
$xy\uparrow$	28.0+11.4i 27.3+7.18i 24.5+5.09i	-85.2i -65.6i -54.5i	28.0+11.4i 27.3+7.18i 24.5+5.09i	85.2i 65.6i 54.5i	-423 -438 -450	
$xy\downarrow$	-85.2i -65.6i -54.5i	28.0-11.4i 27.3-7.18i 24.5-5.09i	85.2i 65.6i 54.5i	28.0-11.4i 27.3-7.18i 24.5-5.09i	0.00 0.00 0.00	-423 -438 -450

ergy differences are estimated as $\Delta_{d-p_{x,y}} \simeq 2.75$ eV and $\Delta_{d-p_z} \simeq 0.92$ eV for the $p_{x,y}$ and p_z orbitals (almost independent of the t_{2g} orbitals), respectively. We note that Δ_{d-p_z} is rather small and in a similar energy scale of the d-p transfers, which might hamper the perturbation theory, but the inclusion of U_p reconciles this situation. In addition, the small Δ_{d-p_z} suggests that further-neighbor transfers can be relevant through the indirect transfers. Indeed, our MLWF analyses find that the second- and third-neighbor transfer integrals, which arise dominantly from the d-p-p-d indirect transfers, include the matrix elements whose magnitudes are comparable to the nearest-neighbor ones at $U_p = 0$. Note, however, that the values are more rapidly reduced by U_p than the nearest-neighbor ones, as they are higher-order contributions in the perturbation theory.

We obtain similar results for $\mathrm{ZnIrO_3}$. The results are summarized in Appendix B. It is noted that the nearest-neighbor xy-yz transfer is one order of magnitude larger for $\mathrm{ZnIrO_3}$ compared to that for $\mathrm{MgIrO_3}$. This is presumably due to the larger buckling of the Ir honeycomb planes in $\mathrm{ZnIrO_3}$.

3. *Effective interaction between $j_{\mathrm{eff}} = 1/2$ pseudospins*

Using the perturbation expansion from the atomic limit of the multiorbital Hubbard model based on the MLWF analysis in Table I, we derive an effective model for the $j_{\mathrm{eff}} = 1/2$ pseudospin degree of freedom (see Sec. II). The effective pseudospin Hamiltonian on the nearest-neighbor z bond is summarized as

$$\mathcal{H}_{ij}^{(z)} = \mathbf{S}_i^{\mathrm{T}} \begin{bmatrix} J & \Gamma & \Gamma' \\ \Gamma & J & \Gamma' \\ \Gamma' & \Gamma' & J+K \end{bmatrix} \mathbf{S}_j, \qquad (2)$$

where $\mathbf{S}_i = (S_i^x, S_i^y, S_i^z)^{\mathrm{T}}$ denotes the pseudospin operator at site i; J, K, Γ, and Γ' denote the coupling constants for the Heisenberg, the Kitaev, and the two different types of symmetric off-diagonal interactions, respectively.

The coupling constants estimated for $\mathrm{MgIrO_3}$ are plotted in Fig. 7 as functions of U_{Ir} with $J_{\mathrm{H}}/U_{\mathrm{Ir}} = 0.1$ and the spin-orbit coupling coefficient $\lambda = 0.4$ eV [26]. The three lines for each coupling constant display the results for $U_p = 0.0$, 0.5, and 1.0 eV. We find that the ferromagnetic Kitaev interaction K is always predominant, and the symmetric off-diagonal interaction Γ is subdominant; the Heisenberg interaction J and the other symmetric off-diagonal interaction Γ' are vanishingly small. This means that the low-energy magnetic property of the spin-orbit coupled Mott insulating state in $\mathrm{MgIrO_3}$ is well described by the model with K and Γ for the nearest-neighbor sites. The model is called the K-Γ model and has been studied in the context of the Kitaev spin liquid, especially for one of the candidates α-$\mathrm{RuCl_3}$ [63, 64].

We note that the magnitude of K is significantly large compared to those for $A_2\mathrm{IrO_3}$ (A = Na and Li) [25–27, 38, 65, 66] when we assume $U_p = 0$, mainly due to the contributions from the large yz-zx transfer in Table I. However, all the coupling constants are substantially reduced by taking into account U_p, as shown in Fig. 7, according to the reduction of the effective transfer integrals.

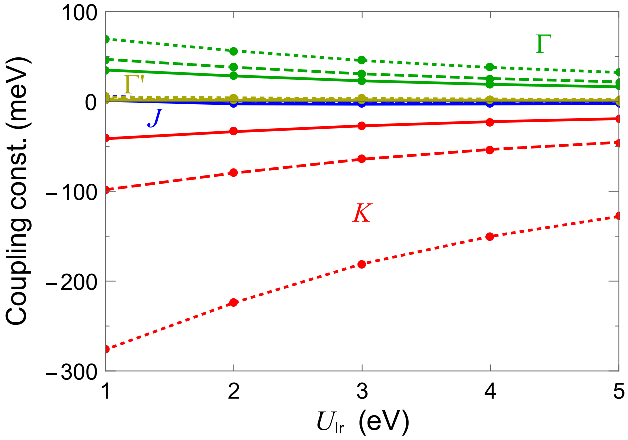

FIG. 7. Coupling constants for the nearest-neighbor pseudospins in $MgIrO_3$ as functions of the Coulomb repulsion at the Ir site, U_{Ir}; see Eq. (2). The Hund's-rule coupling J_{H} and the spin-orbit coupling coefficient λ are set to $J_{\mathrm{H}}/U_{\mathrm{Ir}} = 0.1$ and $\lambda = 0.4$ eV, respectively. The data connected by the blue, red, green, and yellow lines represent the Heisenberg J, Kitaev K, and symmetric off-diagonal couplings Γ and Γ', respectively; the dotted, dashed, and solid lines indicate the data obtained by taking $U_p = 0.0$, 0.5, and 1.0 eV, respectively.

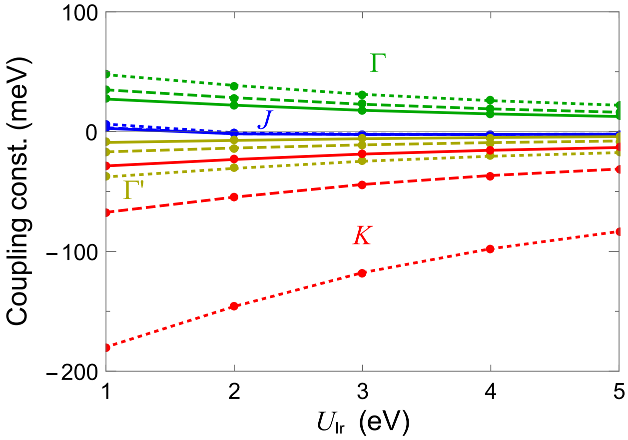

FIG. 8. Coupling constants for the nearest-neighbor pseudospins in $ZnIrO_3$ as functions of U_{Ir} with $J_{\mathrm{H}}/U_{\mathrm{Ir}} = 0.1$ and $\lambda = 0.4$ eV. The notations are common to those in Fig. 7.

For instance, for $U_p = 1$ eV and $U_{\mathrm{Ir}} = 3$ eV, the value of K is reduced to -27.1 meV, which is comparable to that for A_2IrO_3. Although the proper values of U_p and U_{Ir} are unknown, the important conclusion is that the nearest-neighbor magnetic interactions in $MgIrO_3$ can be well described by the K-Γ model irrespective of U_p and U_{Ir}.

As discussed in Sec. III B 2, there are substantial further-neighbor transfers through the indirect contributions via the O $2p$ orbitals. They give rise to sizable further-neighbor exchange interactions, while the coupling constants are reduced by U_p more quickly than the nearest-neighbor ones as they are higher-order processes. For instance, assuming $U_{\mathrm{Ir}} = 3$ eV and $U_p = 1$ eV, the dominant second-neighbor contributions within the same honeycomb layer are the antiferromagnetic $K \simeq 10.3$ meV and the ferromagnetic $J \simeq -8.05$ meV, while the dominant third-neighbor one is the antiferromagnetic $J \simeq 9.06$ meV. We note that the second-neighbor bonds do not have the inversion centers, and hence, include the subdominant Dzyaloshinskii-Moriya interaction, whose energy scale is estimated as $\simeq 5.76$ meV. In addition, we expect contributions from the interlayer couplings through the TiO_6 layer. We speculate that the rather small value of the Curie-Weiss temperature -67.1 K in $MgIrO_3$ could be accounted for by a balance among the exchange couplings including such further-neighbor contributions [19]. While the magnetic structure in the ordered phase is experimentally unknown thus far, it will also be determined under the competing exchange interactions; it is left for future study to precisely construct the effective pseudospin model by determining the values of U_{Ir}, J_{H}, and U_p, and to investigate the stable magnetic structure in the ground state.

TABLE II. Structural parameters of the optimized lattice structure of $MnIrO_3$ with the trigonal $R\bar{3}$ symmetry: the lattice constants a and c for the conventional unit cell shown in Fig. 1(a), the Wyckoff positions of the Mn, Ir, and O ions, and the bond distances d and angles θ for neighboring ions within the same honeycomb layer.

a (Å)	4.9979
c (Å)	13.159
Mn ($6c$)	(0, 0, 0.34535)
Ir ($6c$)	(0, 0, 0.15473)
O ($18f$)	(0.35348, 0.010833, 0.077788)
$d_{\mathrm{Mn-Mn}}$ (Å)	2.9028
$d_{\mathrm{Mn-O}}$ (Å)	1.8828, 1.9803
$\theta_{\mathrm{Mn-O-Mn}}$ (°)	97.398
$d_{\mathrm{Ir-Ir}}$ (Å)	2.9026
$d_{\mathrm{Ir-O}}$ (Å)	2.0133, 2.0700
$\theta_{\mathrm{Ir-O-Ir}}$ (°)	90.596

In the case of $ZnIrO_3$, we plot the effective coupling constants in Fig. 8. The result indicates that, similar to $MgIrO_3$, the magnetic exchange interactions between the neighboring pseudospins are well described by the dominant K and the subdominant Γ, while the other symmetric off-diagonal interaction Γ' has a small but nonnegligible value, in contrast to the case of $MgIrO_3$. This is due to the contribution from the xy-yz transfer discussed in Sec. III B 2.

C. $MnIrO_3$

Finally, we discuss the fictitious compound $MnIrO_3$. Since this compound has not been synthesized thus far, we perform the structural optimization starting from the lattice structure of $MnTiO_3$, as described in Sec. II. The optimal structural data are shown in Table II. We find

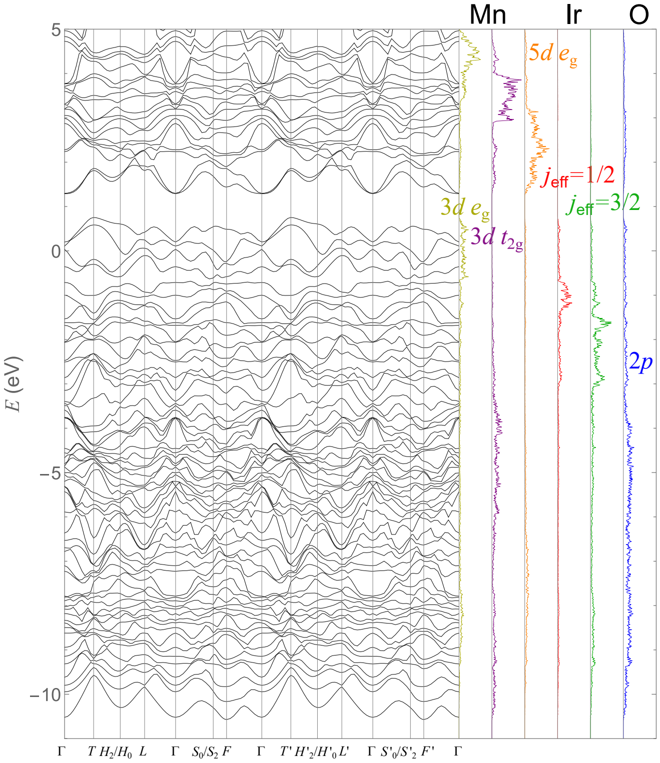

FIG. 9. The electronic band structure of $\mathrm{MnIrO_3}$ obtained by the LDA+SOC+U calculations for the state with c-FM for Mn and ab-FM for Ir with $U_{\rm Mn} = 6$ eV and $U_{\rm Ir} = 3$ eV. The right panels display the projected DOS for each orbital. The Fermi level is set to zero.

that the structure of $\mathrm{MnIrO_3}$ is significantly distorted from that of $\mathrm{MnTiO_3}$. In particular, the Mn-O bond lengths $d_{\rm Mn-O}$ are largely contracted from $d_{\rm Mn-O} = 2.1060$ Å and 2.3026 Å for $\mathrm{MnTiO_3}$ to 1.8828 Å and 1.9803 Å, and the Mn-O-Mn bond angle $\theta_{\rm Mn-O-Mn}$ is largely widened from $\theta_{\rm Mn-O-Mn} = 87.956^\circ$ for $\mathrm{MnTiO_3}$ to 97.398°, as shown in Table II. We speculate that the significant deformation could be related to the difficulty in the bulk synthesis of $\mathrm{MnIrO_3}$.

We study the electronic band structure for the optimal lattice structure by the LDA+SOC+U calculation. We assume $U_{\rm Mn} = 6$ eV and $U_{\rm Ir} = 3$ eV. From energy comparison between different magnetic states for Mn and Ir sites, we find that the state with c-FM for Mn and ab-FM for Ir has the lowest energy, while the magnetic moments are reduced from the $\mathrm{MnTiO_3}$ and $\mathrm{MgIrO_3}$ cases: $|\mathbf{m}_{\rm Mn}| \simeq 3.4\ \mu_{\rm B}$ and $|\mathbf{m}_{\rm Ir}| \simeq 0.008\ \mu_{\rm B}$. The second lowest energy is the state with c-AFM for Mn ($|\mathbf{m}_{\rm Mn}| \simeq 3.4\ \mu_{\rm B}$) and ab-AFM for Ir ($|\mathbf{m}_{\rm Ir}| \simeq 0.005\ \mu_{\rm B}$), whose energy is higher by $\sim$69 meV.

The electronic structure for $\mathrm{MnIrO_3}$ with c-FM for Mn and ab-FM for Ir is shown in Fig. 9. We find that, in contrast to $\mathrm{MnTiO_3}$, $\mathrm{MgIrO_3}$, and $\mathrm{ZnIrO_3}$, the system is metallic and the relevant bands near the Fermi level are composed of the hybridized ones between the Mn $3d$, Ir $5d$, and O $2p$ orbitals. Notably, we find that the valence of Ir ions is considerably different from those for $\mathrm{MgIrO_3}$ and $\mathrm{ZnIrO_3}$. By integrating the projected DOS below the Fermi level, we obtain $\mathrm{Ir}^{2.02+}$ (6.98 $5d$ electrons per Ir ion) for $\mathrm{MnIrO_3}$, which is far from $\mathrm{Ir}^{3.66+}$ (5.34 $5d$ electrons) for $\mathrm{MgIrO_3}$ and $\mathrm{ZnIrO_3}$ at $U_{\rm Ir} = 3$ eV. These results suggest that the low-energy physics of the Ir honeycomb network in $\mathrm{MnIrO_3}$ is not properly described by the effective $j_{\rm eff} = 1/2$ pseudospins which are expected for Ir^{4+}. On the other hand, we find that the valence of Mn ions in $\mathrm{MnIrO_3}$ is similar to that for $\mathrm{MnTiO_3}$: $\mathrm{Mn}^{2.05+}$ for $\mathrm{MnIrO_3}$ and $\mathrm{Mn}^{1.89+}$ for $\mathrm{MnTiO_3}$, both of which are close to Mn^{2+}. Such unusual valence states could also be related to the stability of $\mathrm{MnIrO_3}$.

IV. SUMMARY

To summarize, we have studied the electronic and magnetic properties of the iridium ilmenites $\mathrm{MgIrO_3}$ and $\mathrm{ZnIrO_3}$, in comparison with the conventional antiferromagnetic insulator $\mathrm{MnTiO_3}$. From the *ab initio* calculations, we showed that both Ir compounds have typical electronic band structures of the spin-orbital coupled Mott insulator: the low-energy Ir $5d$ bands are split into the $j_{\rm eff} = 1/2$ doublet and the $j_{\rm eff} = 3/2$ quartet by the spin-orbit coupling, and the half-filled $j_{\rm eff} = 1/2$ doublet is further split by the Coulomb interaction. By using the multiorbital Hubbard model obtained by the MLWF analysis of the band structure, we found that the low-energy magnetic properties are well described by the $j_{\rm eff} = 1/2$ pseudospins interacting with the predominant Kitaev-type bond-dependent interaction and the subdominant symmetric off-diagonal interactions; more specifically, $\mathrm{MgIrO_3}$ and $\mathrm{ZnIrO_3}$ are well approximated by the K-Γ and K-Γ-Γ' models, respectively, while further-neighbor contributions are expected to be relevant as well. In addition, we calculated the electronic band structure for the fictitious compound $\mathrm{MnIrO_3}$ with structural optimization, and showed that it does not provide the $j_{\rm eff} = 1/2$ physics because of the metallic nature and the different ionic state of Ir.

Our results indicate that the iridium ilmenites $\mathrm{MgIrO_3}$ and $\mathrm{ZnIrO_3}$ offer a good platform for exotic magnetism described by the spin-orbital entangled $j_{\rm eff} = 1/2$ moments. The importance of Γ as well as Γ' suggests a similarity to α-$\mathrm{RuCl_3}$ rather than $A_2\mathrm{IrO_3}$ (A = Na and Li), probably due to structural similarity in the lack of cations at the hexagon centers in the honeycomb layers. However, the magnitudes of the coupling constants would be much larger than those for the $4d$-electron compound α-$\mathrm{RuCl_3}$ and comparable to those for the $5d$-electron compounds $A_2\mathrm{IrO_3}$, due to the larger spatial extent of the electron wave functions and the weaker Coulomb interactions. Thus, the Ir ilmenites are the materials that inherit the structural aspect from α-$\mathrm{RuCl_3}$ and the electronic aspect from $A_2\mathrm{IrO_3}$. Our findings would not only be helpful to understand the magnetism in these compounds but also provide a guide toward the realization

TABLE III. Transfer integrals between the Ir t_{2g} orbitals on the nearest-neighbor z bond for $ZnIrO_3$. The notations are common to those in Table I.

	$yz\uparrow$	$yz\downarrow$	$zx\uparrow$	$zx\uparrow$	$xy\uparrow$	$xy\uparrow$
$yz\uparrow$	41.9 77.0 94.7					
$yz\downarrow$	0.00 0.00 0.00	41.9 77.0 94.7				
$zx\uparrow$	1190-12.0i 765-11.2i 553-10.6i	-41.2i -29.9i -23.8i	41.9 77.0 94.7			
$zx\downarrow$	-41.2i -29.9i -23.8i	1190+12.0i 765+11.2i 553+10.6i	0.00 0.00 0.00	41.9 77.0 94.7		
$xy\uparrow$	-258+8.05i -198+5.29i -166+3.84i	-72.6i -58.6i -49.9i	-258+8.05i -198+5.29i -166+3.84i	72.6i 58.6i 49.9i	-312 -344 -366	
$xy\downarrow$	-72.6i -58.6i -49.9i	-258-8.05i -198-5.29i -166-3.84i	72.6i 58.6i 49.9i	-258-8.05i -198-5.29i -166-3.84i	0.00 0.00 0.00	-312 -344 -366

of the Kitaev spin liquid by designing the magnetic interactions.

ACKNOWLEDGMENTS

The crystal structures in Figs. 1(a) and 1(b) were visualized by `VESTA` [67]. Ref. 68 was referred to for the Brillouin zone and the symmetric points in Fig. 1(c). Parts of the numerical calculations have been done using the facilities of the Supercomputer Center, the Institute for Solid State Physics, the University of Tokyo. This work was supported by JST CREST (JP-MJCR18T2), and JSPS KAKENHI Grants No. 19H05825 and No. 20H00122.

Appendix A: HSE approach for $MgIrO_3$

In this Appendix, we present the electronic band structure for the paramagnetic insulating state of $MgIrO_3$ by using the HSE hybrid functional [43]. We adopt the norm-conserving fully-relativistic Perdew-Burke-Ernzerhof type pseudopotentials for all the atoms [69–71] and $8\times8\times8$ Monkhorst-Pack **k**-grids [50] for self-consistent field calculation without the Hubbard correction. In the HSE treatment, we set the Hartree-Fock mixing parameter to $\alpha = 0.05$, which was adopted in the previous calculations for Na_2IrO_3 [72]. The result is shown in Fig. 10. We find that the overall band structure is qualitatively similar to that obtained by the LDA+SOC+U method for a moderate value of $U_{\rm Ir}$ in Sec. III B 1. In particular, there is an energy gap of $E_g \simeq 0.3$ eV between the two $j_{\rm eff} = 1/2$ bands, indicating that the system is a spin-orbit coupled Mott insulator, similar to the LDA+SOC+U results. The comparison suggests that it is reasonable to take $U_{\rm Ir} =$ 2-3 eV in the LDA+SOC+U calculations.

Appendix B: Results for $ZnIrO_3$

In this Appendix, we present the results for $ZnIrO_3$. Figure 11(a) shows the energy comparison between different magnetic states. Similar to $MgIrO_3$ in Sec. III B, $ZnIrO_3$ is a paramagnetic metal at $U_{\rm Ir} = 0$, whose electronic band structure is similar to that for $MgIrO_3$ as shown in Fig. 12. Upon introducing $U_{\rm Ir}$, however, the lowest-energy state is the c-AFM state in contrast to the ab-AFM in $MgIrO_3$, while the energy difference ΔE to the second-lowest state, the ab-AFM, is not so large (less than 0.01 eV), as shown in Fig. 11(a). The result indicates that $ZnIrO_3$ has an out-of-plane magnetic anisotropy, although the experiment shows an easy-plane anisotropy [19]. Nonetheless, the behaviors of the energy gap and the antiferromagnetic moment are similar to those for $MgIrO_3$, as shown in Figs. 11(b) and 11(c), respectively.

Figure 13 shows the electronic band structure of the c-AFM insulating state for $ZnIrO_3$. Again, the result is similar to that for $MgIrO_3$: the energy gap opens between the two $j_{\rm eff} = 1/2$ bands, realizing the spin-orbit

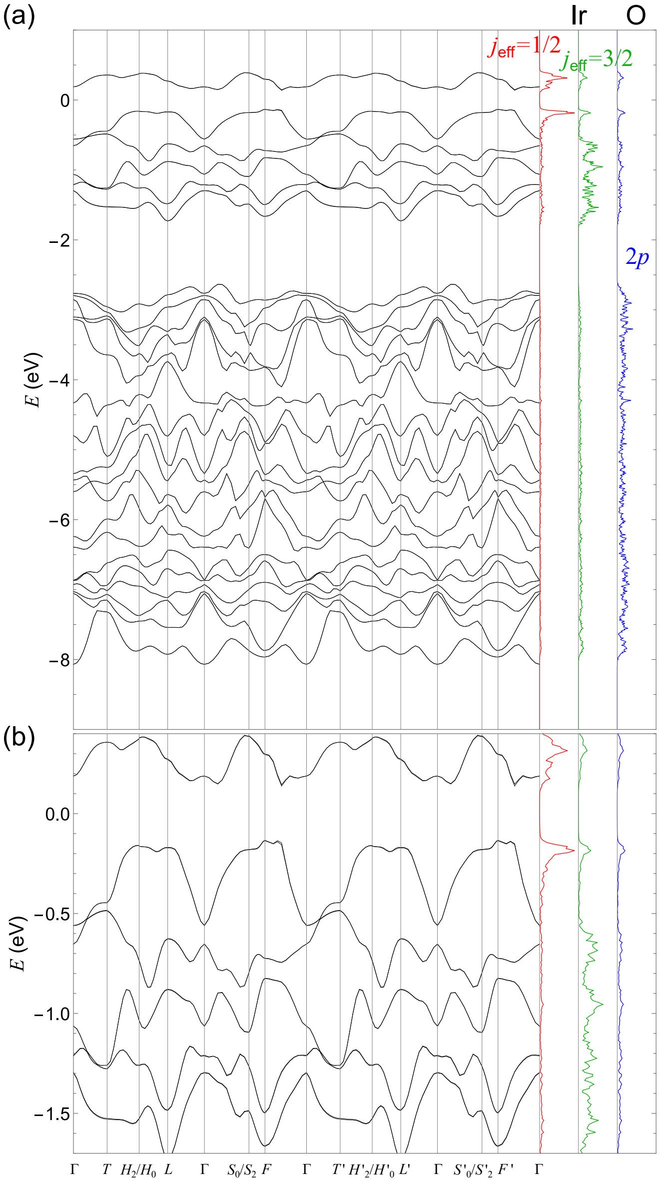

FIG. 10. The electronic band structure for the paramagnetic state of $\mathrm{MgIrO_3}$ obtained by using the HSE hybrid functional with the Hartree-Fock mixing parameter $\alpha = 0.05$. The notations are common to those in Fig. 6.

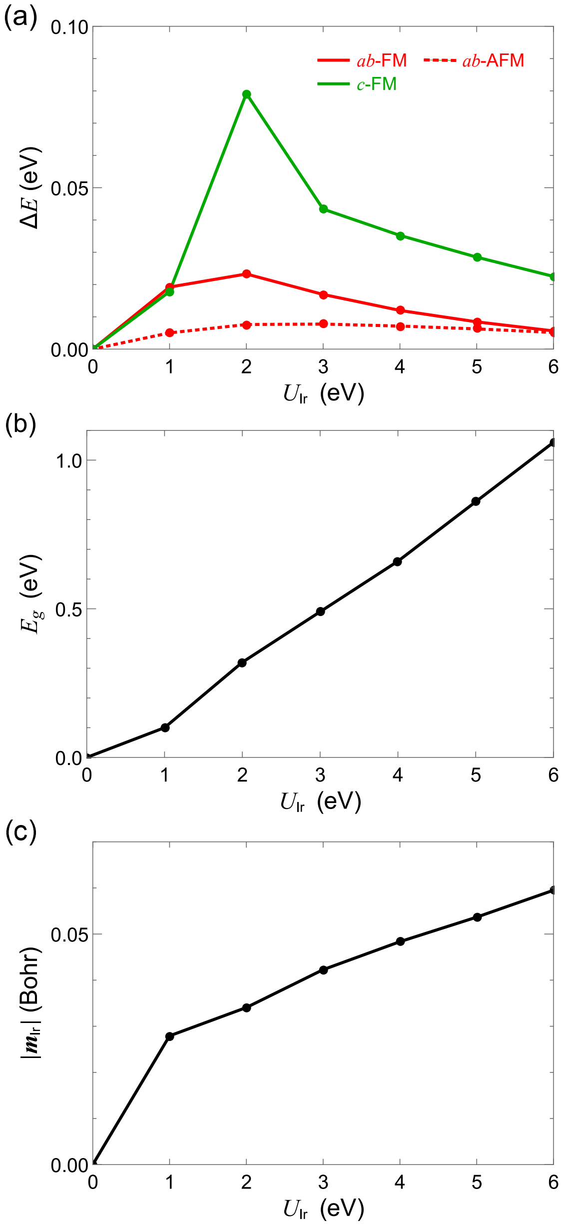

FIG. 11. (a) Energy measured from the c-AFM state in $\mathrm{ZnIrO_3}$ as a function of the Coulomb repulsion at the Ir site, $U_{\rm Ir}$, obtained by the LDA+SOC+U calculations. (b) The energy gap and (c) the antiferromagnetic moment at the Ir site in the c-AFM state.

coupled Mott insulating state. In this case, we perform the MLWF analysis including the Zn $3d$ orbitals as mentioned in Sec. II, since the energy levels overlap with those for the O $2p$ orbitals. We plot the obtained tight-binding band structure in Fig. 12, which well reproduce the *ab initio* result. In Table III, we show the effective transfer integrals for the Ir t_{2g} orbitals on the nearest-neighbor z bond estimated from the MLWF analysis. In the calculations, we use $\Delta_{d-p_{x,y}} \simeq 3.09$ eV and $\Delta_{d-p_z} \simeq 1.02$ eV estimated from the MLWF analysis. Similar to the case of $\mathrm{MgIrO_3}$, the dominant effective transfer is between the yz and zx orbitals. Meanwhile, the xy-yz transfer has much larger value than that for $\mathrm{MgIrO_3}$, presumably due to the larger buckling of the Ir honeycomb planes, as mentioned in the main text; the height difference in the c direction between two neighboring Ir sites is $1.3341 \times 10^{-2}c$ for $\mathrm{ZnIrO_3}$, while it is $1.5734 \times 10^{-3}c$ for $\mathrm{MgIrO_3}$. The estimates of the effective coupling constants between the pseudospins are shown in Fig. 8.

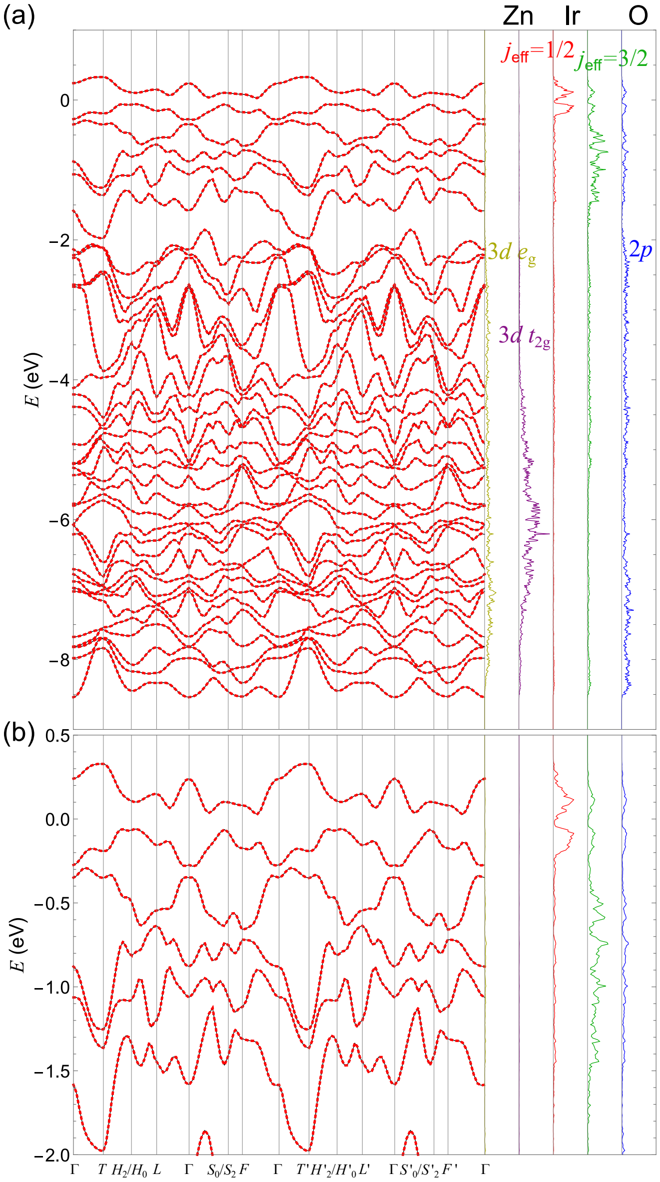

FIG. 12. The electronic band structure of $\mathrm{ZnIrO_3}$ obtained by the LDA calculations ($U_{\rm Ir} = 0$) for the paramagnetic metallic state. The notations are common to those in Fig. 5.

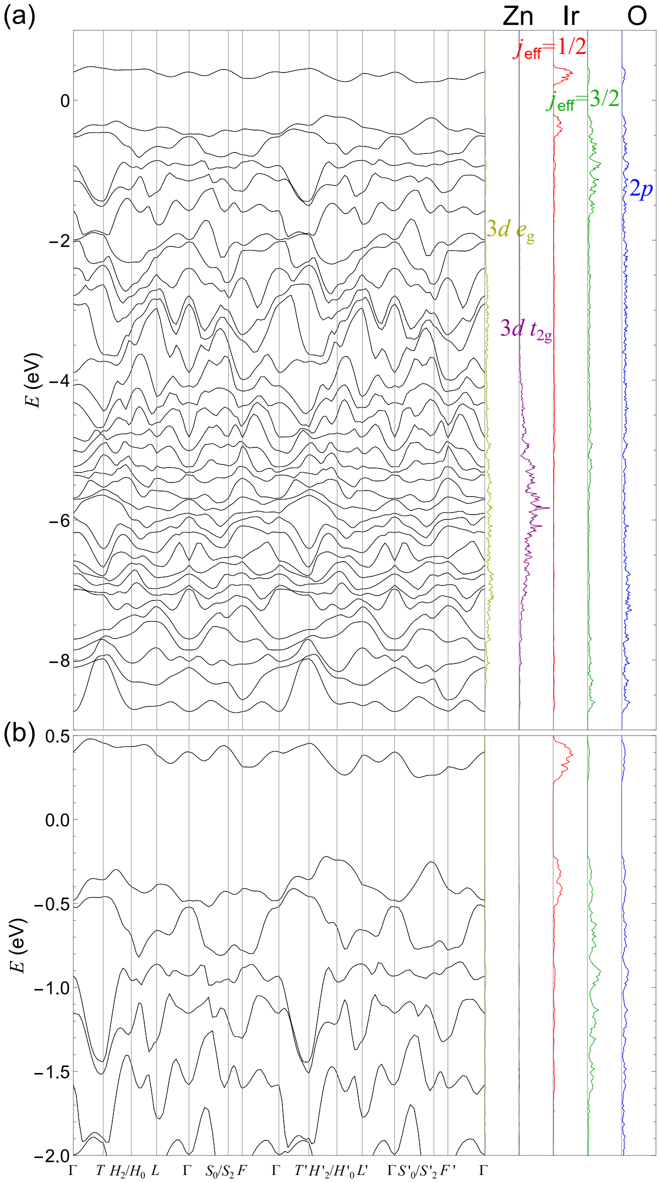

FIG. 13. The electronic band structure of $\mathrm{ZnIrO_3}$ obtained by the LDA+SOC+U calculations for the c-AFM state with $U_{\rm Ir} = 3$ eV. The notations are common to those in Fig. 6.

---

[1] Y. Ishikawa and S.-I. Akimoto, Magnetic property and crystal chemistry of ilmenite (MeTio$_3$) and hematite (αFe$_2$O$_3$) system I. crystal chemistry, J. Phys. Soc. Japan **13**, 1110 (1958).

[2] G. S. Heller, J. J. Stickler, S. Kern, and A. Wold, Antiferromagnetism in NiTiO$_3$, J. Appl. Phys. **34**, 1033 (1963).

[3] R. E. Newnham, J. H. Fang, and R. P. Santoro, Crystal structure and magnetic properties of CoTiO$_3$, Acta Crystallogr. **17**, 240 (1964).

[4] G. Shirane, S. J. Pickart, and Y. Ishikawa, Neutron diffraction study of antiferromagnetic MnTiO$_3$ and NiTiO$_3$, J. Phys. Soc. Jpn. **14**, 1352 (1959).

[5] J. J. Stickler, S. Kern, A. Wold, and G. S. Heller, Magnetic resonance and susceptibility of several ilmenite powders, Phys. Rev. **164**, 765 (1967).

[6] J. Akimitsu, Y. Ishikawa, and Y. Endoh, On the two-dimensional antiferromagnetic character of MnTiO$_3$, Solid State Commun. **8**, 87 (1970).

[7] J. Akimitsu and Y. Ishikawa, Magnetic critical behavior of a quasi two-dimensional antiferromagnet MnTiO$_3$, J. Phys. Soc. Japan **42**, 462 (1977).

[8] H. Watanabe, H. Yamauchi, and H. Takei, Magnetic anisotropies in mTiO$_3$ (m = Co, Ni), J. Magn. Magn. Mater. **15-18**, 549 (1980).

[9] Y. Yamaguchi, H. Kato, H. Takei, A. Goldman, and G. Shirane, Re-examination of the magnetic structure of FeTiO$_3$, Solid State Commun. **59**, 865 (1986).

[10] K. Dey, S. Sauerland, J. Werner, Y. Skourski, M. Abdel-Hafiez, R. Bag, S. Singh, and R. Klingeler, Magnetic phase diagram and magnetoelastic coupling of NiTiO$_3$, Phys. Rev. B **101**, 195122 (2020).

[11] A. Ito, H. Aruga, E. Torikai, M. Kikuchi, Y. Syono, and H. Takei, Time-dependent phenomena in a short-range ising spin-glass, Fe$_{0.5}$Mn$_{0.5}$TiO$_3$, Phys. Rev. Lett. **57**, 483 (1986).

[12] H. Yoshizawa, S. Mitsuda, H. Aruga, and A. Ito, Mixed phase of spin-glass ordering and antiferromagnetism in an Ising system, Fe$_x$Mn$_{1-x}$TiO$_3$, Phys. Rev. Lett. **59**, 2364 (1987).

[13] H. Yoshizawa, S. Mitsuda, H. Aruga, and A. Ito, Reentrant spin-glass transition and a mixed phase in an Ising system Fe$_x$Mn$_{1-x}$TiO$_3$, J. Phys. Soc. Japan **58**, 1416 (1989).

[14] H. Kawano, H. Yoshizawa, A. Ito, and K. Motoya, Two successive spin glass transitions in nondiluted Heisenberg-like spin glass Ni$_{0.42}$Mn$_{0.58}$TiO$_3$, J. Phys. Soc. Japan **62**, 2575 (1993).

[15] H. Yoshizawa, H. Mori, H. Kawano, H. Aruga-Katori, S. Mituta, and A. Ito, Phase diagram of a reentrant ising spin glass Fe$_{0.6}$Mn$_{0.4}$TiO$_3$ on the magnetic field-temperature plane, J. Phys. Soc. Japan **63**, 3145 (1994).

[16] Y. Yamaguchi, T. Nakano, Y. Nozue, and T. Kimura, Magnetoelectric effect in an xy-like spin glass system Ni$_x$Mn$_{1-x}$TiO$_3$, Phys. Rev. Lett. **108**, 057203 (2012).

[17] J. K. Harada, L. Balhorn, J. Hazi, M. C. Kemei, and R. Seshadri, Magnetodielectric coupling in the ilmenites mTiO$_3$ (m =Co, Ni), Phys. Rev. B **93**, 104404 (2016).

[18] T. Sato, N. Abe, S. Kimura, Y. Tokunaga, and T.-h. Arima, Magnetochiral dichroism in a collinear antiferromagnet with no magnetization, Phys. Rev. Lett. **124**, 217402 (2020).

[19] Y. Haraguchi, C. Michioka, A. Matsuo, K. Kindo, H. Ueda, and K. Yoshimura, Magnetic ordering with an xy-like anisotropy in the honeycomb lattice iridates ZnIrO$_3$ and MgIrO$_3$ synthesized via a metathesis reaction, Phys. Rev. Materials **2**, 054411 (2018).

[20] Y. Haraguchi and H. A. Katori, Strong antiferromagnetic interaction owing to a large trigonal distortion in the spin-orbit-coupled honeycomb lattice iridate CdIrO$_3$, Phys. Rev. Materials **4**, 044401 (2020).

[21] J. Chaloupka, G. Jackeli, and G. Khaliullin, Kitaev-Heisenberg model on a honeycomb lattice: Possible exotic phases in iridium oxides A_2IrO$_3$, Phys. Rev. Lett. **105**, 027204 (2010).

[22] Y. Singh and P. Gegenwart, Antiferromagnetic Mott insulating state in single crystals of the honeycomb lattice material Na$_2$IrO$_3$, Phys. Rev. B **82**, 064412 (2010).

[23] Y. Singh, S. Manni, J. Reuther, T. Berlijn, R. Thomale, W. Ku, S. Trebst, and P. Gegenwart, Relevance of the Heisenberg-Kitaev model for the honeycomb lattice iridates A_2IrO$_3$, Phys. Rev. Lett. **108**, 127203 (2012).

[24] K. Foyevtsova, H. O. Jeschke, I. I. Mazin, D. I. Khomskii, and R. Valentí, *Ab initio* analysis of the tight-binding parameters and magnetic interactions in Na$_2$IrO$_3$, Phys. Rev. B **88**, 035107 (2013).

[25] V. M. Katukuri, S. Nishimoto, V. Yushankhai, A. Stoyanova, H. Kandpal, S. Choi, R. Coldea, I. Rousochatzakis, L. Hozoi, and J. van den Brink, Kitaev interactions between $j = 1/2$ moments in honeycomb Na$_2$IrO$_3$ are large and ferromagnetic: insights from *ab initio* quantum chemistry calculations, New J. Phys. **16**, 013056 (2014).

[26] Y. Yamaji, Y. Nomura, M. Kurita, R. Arita, and M. Imada, First-principles study of the honeycomb-lattice iridates Na$_2$IrO$_3$ in the presence of strong spin-orbit interaction and electron correlations, Phys. Rev. Lett. **113**, 107201 (2014).

[27] S. M. Winter, Y. Li, H. O. Jeschke, and R. Valentí, Challenges in design of Kitaev materials: Magnetic interactions from competing energy scales, Phys. Rev. B **93**, 214431 (2016).

[28] F. Freund, S. C. Williams, R. D. Johnson, R. Coldea, P. Gegenwart, and A. Jesche, Single crystal growth from separated educts and its application to lithium transition-metal oxides, Sci. Rep. **6**, 35362 (2016).

[29] S. M. Winter, A. A. Tsirlin, M. Daghofer, J. van den Brink, Y. Singh, P. Gegenwart, and R. Valentí, Models and materials for generalized Kitaev magnetism, J. Phys.: Condens. Matter **29**, 493002 (2017).

[30] H. Takagi, T. Takayama, G. Jackeli, G. Khaliullin, and S. E. Nagler, Concept and realization of Kitaev quantum spin liquids, Nat. Rev. Phys. **1**, 264 (2019).

[31] Y. Motome and J. Nasu, Hunting Majorana fermions in Kitaev magnets, J. Phys. Soc. Japan **89**, 012002 (2020).

[32] B. J. Kim, H. Jin, S. J. Moon, J.-Y. Kim, B.-G. Park, C. S. Leem, J. Yu, T. W. Noh, C. Kim, S.-J. Oh, J.-H. Park, V. Durairaj, G. Cao, and E. Rotenberg, Novel $J_{\text{eff}} = 1/2$ Mott state induced by relativistic spin-orbit coupling in Sr$_2$IrO$_4$, Phys. Rev. Lett. **101**, 076402 (2008).

[33] R. Comin, G. Levy, B. Ludbrook, Z.-H. Zhu, C. N. Veenstra, J. A. Rosen, Y. Singh, P. Gegenwart, D. Stricker, J. N. Hancock, D. van der Marel, I. S. Elfimov, and A. Damascelli, Na$_2$IrO$_3$ as a novel relativistic Mott insu-

lator with a 340-mev gap, Phys. Rev. Lett. **109**, 266406 (2012).

[34] C. H. Sohn, H.-S. Kim, T. F. Qi, D. W. Jeong, H. J. Park, H. K. Yoo, H. H. Kim, J.-Y. Kim, T. D. Kang, D.-Y. Cho, G. Cao, J. Yu, S. J. Moon, and T. W. Noh, Mixing between $J_{\rm eff}=\frac{1}{2}$ and $\frac{3}{2}$ orbitals in Na_2IrO_3: A spectroscopic and density functional calculation study, Phys. Rev. B **88**, 085125 (2013).

[35] S. Hwan Chun, J.-W. Kim, J. Kim, H. Zheng, C. C. Stoumpos, C. D. Malliakas, J. F. Mitchell, K. Mehlawat, Y. Singh, Y. Choi, T. Gog, A. Al-Zein, M. M. Sala, M. Krisch, J. Chaloupka, G. Jackeli, G. Khaliullin, and B. J. Kim, Direct evidence for dominant bond-directional interactions in a honeycomb lattice iridate Na_2IrO_3, Nat. Phys. **11**, 462 (2015).

[36] S. D. Das, S. Kundu, Z. Zhu, E. Mun, R. D. McDonald, G. Li, L. Balicas, A. McCollam, G. Cao, J. G. Rau, H.-Y. Kee, V. Tripathi, and S. E. Sebastian, Magnetic anisotropy of the alkali iridate Na_2IrO_3 at high magnetic fields: Evidence for strong ferromagnetic Kitaev correlations, Phys. Rev. B **99**, 081101(R) (2019).

[37] F. Ye, S. Chi, H. Cao, B. C. Chakoumakos, J. A. Fernandez-Baca, R. Custelcean, T. F. Qi, O. B. Korneta, and G. Cao, Direct evidence of a zigzag spin-chain structure in the honeycomb lattice: A neutron and x-ray diffraction investigation of single-crystal Na_2IrO_3, Phys. Rev. B **85**, 180403(R) (2012).

[38] S. C. Williams, R. D. Johnson, F. Freund, S. Choi, A. Jesche, I. Kimchi, S. Manni, A. Bombardi, P. Manuel, P. Gegenwart, and R. Coldea, Incommensurate counterrotating magnetic order stabilized by Kitaev interactions in the layered honeycomb α-Li_2IrO_3, Phys. Rev. B **93**, 195158 (2016).

[39] X. Liu, T. Berlijn, W.-G. Yin, W. Ku, A. Tsvelik, Y.-J. Kim, H. Gretarsson, Y. Singh, P. Gegenwart, and J. P. Hill, Long-range magnetic ordering in Na_2IrO_3, Phys. Rev. B **83**, 220403(R) (2011).

[40] K. Miura, K. Fujiwara, K. Nakayama, R. Ishikawa, N. Shibata, and A. Tsukazaki, Stabilization of a honeycomb lattice of IrO_6 octahedra by formation of ilmenite-type superlattices in $MnTiO_3$, Commun. Mater. **1**, 55 (2020).

[41] G. H. Wannier, The structure of electronic excitation levels in insulating crystals, Phys. Rev. **52**, 191 (1937).

[42] A. A. Mostofi, J. R. Yates, G. Pizzi, Y.-S. Lee, I. Souza, D. Vanderbilt, and N. Marzari, An updated version of wannier90: A tool for obtaining maximally-localised Wannier functions, Comput. Phys. Commun. **185**, 2309 (2014).

[43] J. Heyd, G. E. Scuseria, and M. Ernzerhof, Hybrid functionals based on a screened Coulomb potential, J. Chem. Phys. **118**, 8207 (2003).

[44] P. Giannozzi, O. Andreussi, T. Brumme, O. Bunau, M. B. Nardelli, M. Calandra, R. Car, C. Cavazzoni, D. Ceresoli, M. Cococcioni, N. Colonna, I. Carnimeo, A. D. Corso, S. de Gironcoli, P. Delugas, R. A. D. Jr., A. Ferretti, A. Floris, G. Fratesi, G. Fugallo, R. Gebauer, U. Gerstmann, F. Giustino, T. Gorni, J. Jia, M. Kawamura, H.-Y. Ko, A. Kokalj, E. Küçükbenli, M. Lazzeri, M. Marsili, N. Marzari, F. Mauri, N. L. Nguyen, H.-V. Nguyen, A. O. de-la Roza, L. Paulatto, S. Poncé, D. Rocca, R. Sabatini, B. Santra, M. Schlipf, A. P. Seitsonen, A. Smogunov, I. Timrov, T. Thonhauser, P. Umari, N. Vast, X. Wu, and S. Baroni, Advanced capabilities for materials modelling with quantum ESPRESSO, J. Phys.: Condens. Matter **29**, 465901 (2017).

[45] J. P. Perdew and A. Zunger, Self-interaction correction to density-functional approximations for many-electron systems, Phys. Rev. B **23**, 5048 (1981).

[46] P. E. Blöchl, Projector augmented-wave method, Phys. Rev. B **50**, 17953 (1994).

[47] A. D. Corso, Pseudopotentials periodic table: From H to Pu, Comput. Mater. Sci. **95**, 337 (2014).

[48] R. P. Liferovich and R. H. Mitchell, Stabilization of a honeycomb lattice of IrO_6 octahedra by formation of ilmenite-type superlattices in $MnTiO_3$, Phys. Chem. Miner. **32**, 442 (2005).

[49] C. G. Broyden, The convergence of a class of double-rank minimization algorithms 1. General considerations, IMA J. Appl. Math. **6**, 76 (1970).

[50] H. J. Monkhorst and J. D. Pack, Special points for Brillouin-zone integrations, Phys. Rev. B **13**, 5188 (1976).

[51] A. I. Liechtenstein, V. I. Anisimov, and J. Zaanen, Density-functional theory and strong interactions: Orbital ordering in Mott-Hubbard insulators, Phys. Rev. B **52**, R5467 (1995).

[52] H.-S. Kim and H.-Y. Kee, Crystal structure and magnetism in α-$RuCl_3$: An *ab initio* study, Phys. Rev. B **93**, 155143 (2016).

[53] Y. Sugita, Y. Kato, and Y. Motome, Antiferromagnetic Kitaev interactions in polar spin-orbit Mott insulators, Phys. Rev. B **101**, 100410(R) (2020).

[54] S.-H. Jang, R. Sano, Y. Kato, and Y. Motome, Antiferromagnetic Kitaev interaction in f-electron based honeycomb magnets, Phys. Rev. B **99**, 241106(R) (2019).

[55] S.-H. Jang, R. Sano, Y. Kato, and Y. Motome, Computational design of f-electron Kitaev magnets: Honeycomb and hyperhoneycomb compounds A_2PrO_3 (A = alkali metals, Phys. Rev. Materials **4**, 104420 (2020).

[56] M. Enhessari, A. Parviz, E. Karamali, and K. Ozaee, Synthesis, characterisation and optical properties of $MnTiO_3$ nanopowders, J. Exp. Nanosci. **7**, 327 (2012).

[57] X. Deng, W. Lu, H. Wang, H. Huang, and J. Dai, Electronic, magnetic and dielectric properties of multiferroic $MnTiO_3$, J. Mater. Res. **27**, 1421 (2012).

[58] K. W. Plumb, J. P. Clancy, L. J. Sandilands, V. V. Shankar, Y. F. Hu, K. S. Burch, H.-Y. Kee, and Y.-J. Kim, α-$RuCl_3$: A spin-orbit assisted Mott insulator on a honeycomb lattice, Phys. Rev. B **90**, 041112(R) (2014).

[59] R. D. Johnson, S. C. Williams, A. A. Haghighirad, J. Singleton, V. Zapf, P. Manuel, I. I. Mazin, Y. Li, H. O. Jeschke, R. Valentí, and R. Coldea, Monoclinic crystal structure of α-$RuCl_3$ and the zigzag antiferromagnetic ground state, Phys. Rev. B **92**, 235119 (2015).

[60] S. Sarikurt, Y. Kadioglu, F. Ersan, E. Vatansever, O. Üzengi Aktürk, Y. Yüksel, Ü. Akıncı, and E. Aktürk, Electronic and magnetic properties of monolayer α-$RuCl_3$: a first-principles and Monte Carlo study, Phys. Chem. Chem. Phys. **20**, 997 (2018).

[61] J. P. Clancy, H. Gretarsson, J. A. Sears, Y. Singh, S. Desgreniers, K. Mehlawat, S. Layek, G. K. Rozenberg, Y. Ding, M. H. Upton, D. Casa, N. Chen, J. Im, Y. Lee, R. Yadav, L. Hozoi, D. Efremov, J. van den Brink, and Y.-J. Kim, Pressure-driven collapse of the relativistic electronic ground state in a honeycomb iridate, npj Quantum Mater. **3**, 35 (2018).

[62] G. Jackeli and G. Khaliullin, Mott insulators in the strong spin-orbit coupling limit: From Heisenberg to a quantum compass and Kitaev models, Phys. Rev. Lett. **102**, 017205 (2009).

[63] J. G. Rau, E. K.-H. Lee, and H.-Y. Kee, Generic spin model for the honeycomb iridates beyond the Kitaev limit, Phys. Rev. Lett. **112**, 077204 (2014).

[64] J. Rusnačko, D. Gotfryd, and J. Chaloupka, Kitaev-like honeycomb magnets: Global phase behavior and emergent effective models, Phys. Rev. B **99**, 064425 (2019).

[65] S. K. Choi, R. Coldea, A. N. Kolmogorov, T. Lancaster, I. I. Mazin, S. J. Blundell, P. G. Radaelli, Y. Singh, P. Gegenwart, K. R. Choi, S.-W. Cheong, P. J. Baker, C. Stock, and J. Taylor, Spin waves and revised crystal structure of honeycomb iridate $\mathrm{Na_2IrO_3}$, Phys. Rev. Lett. **108**, 127204 (2012).

[66] S. N. Gupta, P. V. Sriluckshmy, K. Mehlawat, A. Balodhi, D. K. Mishra, S. R. Hassan, T. V. Ramakrishnan, D. V. S. Muthu, Y. Singh, and A. K. Sood, Raman signatures of strong Kitaev exchange correlations in $\mathrm{(Na_{1-x}Li_x)_2IrO_3}$: Experiments and theory, Europhys. Lett. **114**, 47004 (2016).

[67] K. Momma and F. Izumi, VESTA 3 for three-dimensional visualization of crystal, volumetric and morphology data, J. Appl. Crystallogr. **44**, 1272 (2011).

[68] Y. Hinuma, G. Pizzi, Y. Kumagai, F. Oba, and I. Tanaka, Band structure diagram paths based on crystallography, Comput. Mater. Sci. **128**, 140 (2017).

[69] D. R. Hamann, M. Schlüter, and C. Chiang, Norm-conserving pseudopotentials, Phys. Rev. Lett. **43**, 1494 (1979).

[70] J. P. Perdew, K. Burke, and M. Ernzerhof, Generalized gradient approximation made simple, Phys. Rev. Lett. **77**, 3865 (1996).

[71] P. Scherpelz, M. Govoni, I. Hamada, and G. Galli, Implementation and validation of fully relativistic *GW* calculations: Spinorbit coupling in molecules, nanocrystals, and solids, J. Chem. Theory Comput. **12**, 3523 (2016).

[72] H.-J. Kim, J.-H. Lee, and J.-H. Cho, Antiferromagnetic Slater insulator phase of $\mathrm{Na_2IrO_3}$, Sci. Rep. **4**, 5253 (2014).